ACS Partner Journal
PRECISION CHEMISTRY
pubs.acs.org/PrecisionChem

Article

Water-Mediated Proton Hopping Mechanisms at the $SnO_2(110)/H_2O$ Interface from Ab Initio Deep Potential Molecular Dynamics

Mei Jia,[#] Yong-Bin Zhuang,[#] Feng Wang, Chao Zhang, and Jun Cheng*

Cite This: *Precis. Chem.* 2024, 2, 644−654

Read Online

ACCESS | Metrics & More | Article Recommendations | Supporting Information

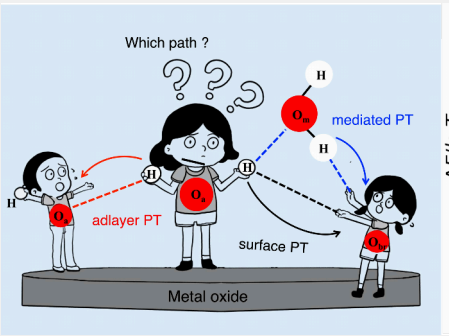

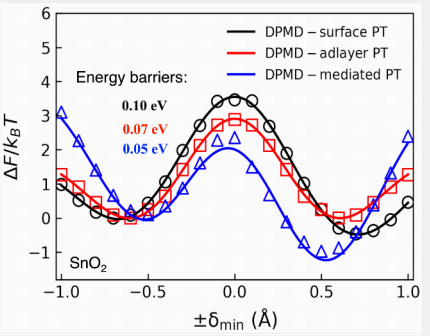

ABSTRACT: The interfacial proton transfer (PT) reaction on the metal oxide surface is an important step in many chemical processes including photoelectrocatalytic water splitting, dehydrogenation, and hydrogen storage. The investigation of the PT process, in terms of thermodynamics and kinetics, has received considerable attention, but the individual free energy barriers and solvent effects for different PT pathways on rutile oxide are still lacking. Here, by applying a combination of ab initio and deep potential molecular dynamics methods, we have studied interfacial PT mechanisms by selecting the rutile $SnO_2(110)/H_2O$ interface as an example of an oxide with the characteristic of frequently interfacial PT processes. Three types of PT pathways among the interfacial groups are found, i.e., proton transfer from terminal adsorbed water to bridge oxygen directly (surface-PT) or via a solvent water (mediated-PT), and proton hopping between two terminal groups (adlayer PT). Our simulations reveal that the terminal water in mediated-PT prefers to point toward the solution and forms a shorter H-bond with the assisted solvent water, leading to the lowest energy barrier and the fastest relative PT rate. In particular, it is found that the full solvation environment plays a crucial role in water-mediated proton conduction, while having little effect on direct PT reactions. The PT mechanisms on aqueous rutile oxide interfaces are also discussed by comparing an oxide series composed of SnO_2, TiO_2, and IrO_2. Consequently, this work provides valuable insights into the ability of a deep neural network to reproduce the ab initio potential energy surface, as well as the PT mechanisms at such oxide/liquid interfaces, which can help understand the important chemical processes in electrochemistry, photoelectrocatalysis, colloid science, and geochemistry.

KEYWORDS: *Proton transfer mechanism, ab initio molecular dynamics, deep potential molecular dynamics, rutile oxide, machine learning, solvation effect, free energy*

INTRODUCTION

Metal oxide electrode materials are ubiquitous in a number of applications, including electrochemistry,[1] photoelectrocatalysis,[2] geochemistry,[3] biochemistry,[4] and colloid science.[5,6] When the electrode is exposed to humid environments or immersed in solution at working conditions, water species, i.e., protons and hydroxyl groups, are always adsorbed on the active functional sites of metal oxide surfaces.[7−11] The interfacial proton transfer (PT) reaction among the water species is a key elementary step in many chemical processes,[12−14] including photocatalytic[15] or electrochemical water splitting,[16] catalytic hydrogen evolution and reforming,[17] photocatalytic dehydrogenation,[18] and hydrogen storage.[19] Therefore, the investigation of the PT process, in terms of kinetics and thermodynamics, has received considerable attention both from experiments and theoretical simulations in recent years.

Despite traditional approaches, i.e., vibrational spectroscopy[20] and X-ray scattering methods,[21] which have been applied to explore the interfacial water, advanced experimental techniques such as in situ X-ray photoelectron spectroscopy (XPS),[22,23] sum-frequency-generation spectroscopy

Received: July 4, 2024
Revised: August 19, 2024
Accepted: August 20, 2024
Published: September 18, 2024

https://doi.org/10.1021/prechem.4c00056
Precis. Chem. 2024, 2, 644−654

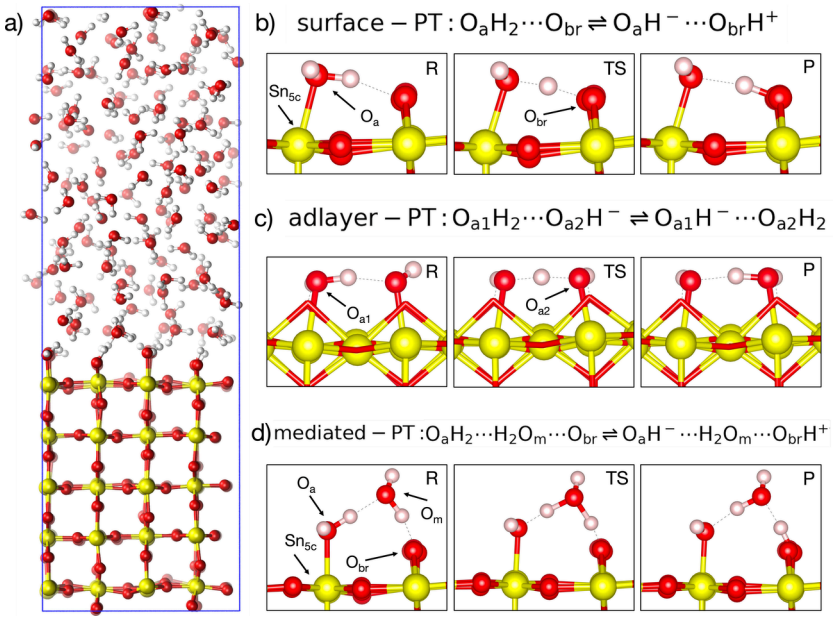

Figure 1. (a) Molecular dynamics model of the $SnO_2(110)/H_2O$ interface. Three proton transfer pathways at the $SnO_2(110)/H_2O$ interface (b) surface-PT: proton transfer between terminal adsorbed water molecule O_aH_2 and bridging oxygen O_{br}, (c) adlayer-PT: proton hopping between terminal adsorbed $O_{a1}H_2$ and another terminal $O_{a2}H^-$, (d) mediated-PT: proton transfer between O_aH_2 and O_{br} via a solvent water H_2O_m.

(SFG),[24−27] in situ Raman spectroscopy,[28−30] and scanning tunneling microscopy (STM)[31−33] further provide the elemental composition, and structural and dynamical properties of oxide/liquid interfaces at the molecular level. However, it is still challenging to probe the microscopic structures and identify the dynamic interfacial proton hopping events with sufficient atomic resolution, especially in distinguishing the different pathways of PT reactions.

Alternatively, ab initio molecular dynamics (AIMD) can provide valuable interfacial information at the atomistic scale.[34−41] Compared to static density functional theory (DFT) optimizations, implicit solvation model or other classical molecular dynamics simulations,[42−44] AIMD simulations have one great advantage that they include the all-atom method, treating solute and solvent at the same level of electronic structure and computing the electronic structure from first-principles calculation.[45] Hence, it is appropriate to investigate interfacial PT events, which involve the breaking and forming of O−H bonds dynamically, with AIMD simulations.

However, it is difficult to reach the equilibration of PT dynamics among the interfacial species in the picosecond (ps) time scale from AIMD simulations, especially for the slow PT processes at the metal oxide surfaces.[46] Both the expensive computational cost of a heterogeneous supercell and the limitation of time scale for AIMD calculations make the study of interfacial PT events quite difficult. Fortunately, the fledged machine-learned (ML) potential techniques dramatically extend both the supercell size and time scale for the MD simulations.[46−54] Assisted by the deep neural network (DNN), ML potentials are trained using configurations and corresponding energies and forces from DFT for potential energy surface (PES).[38,47,51,52] The application of ML potentials significantly accelerates MD simulations and keeps ab initio accuracy.

In the case of large free-energy barriers related to slow and rare interfacial PT events, it calls for enhanced sampling techniques, such as umbrella sampling[51,55] and metadynamics,[56−60] which increase the relative probability of rare configurations as well as accelerating the PT events more frequently. Currently, both the DNN based MD simulations and enhanced sampling MD simulations have been successfully applied to investigate various oxide/liquid interfaces, for example, Selloni and Cheng have reported aqueous rutile $TiO_2(110)$, (100), and (011),[58,61] anatase $TiO_2(100)$, (101), and (110),[51,58] and $IrO_2(110)$ interfaces,[59] Nakayama has studied aqueous $CeO_2(111)$ and (110) interfaces,[60] and Behler has reported the water-ZnO(1010) interface.[38,62] The interfacial structural properties, dynamic behavior, H-bond networks, and proton transfer pathways, i.e., direct and indirect PT reactions between interfacial species, have been demonstrated in these works. However, individual free energy barriers and solvent effects of different PT pathways on rutile oxide are still lacking.

A previous work has shown that the surface groups $Sn_{5c}OH_2$ and Sn_2OH^+ on rutile $SnO_2(110)$ have close pK_a values, and the terminal adsorbed water dissociates spontaneously and frequently.[63] To explore the molecular picture of microscopic structure, PT pathways, and solvent effects on the rutile oxide surface, SnO_2 can serve as a model system with fast PT processes. Currently, SnO_2-based materials have been widely applied for many technological fields such as solar batteries,[64] catalysis,[65] lithium-ion batteries,[66] and gas sensors,[67] due to their nontoxic nature, abundance in the Earth's crust, and low cost.

In this study, we train and validate deep potentials and then perform Deep Potential Molecular Dynamics (DPMD) simulations for the $SnO_2(110)/H_2O$ interface. We analyze the microscopic structure and find three types of PT pathways among the interfacial species at the $SnO_2(110)/H_2O$ interface. Additionally, we discuss the free energy landscapes and relative PT rates for these PT reactions. It is followed by the investigation of full solvation effects on interfacial PT reactions via comparing climbing image nudged elastic band (CI-NEB) calculations for a monolayer of adsorbed water. We also

https://doi.org/10.1021/prechem.4c00056
Precis. Chem. 2024, 2, 644−654

calculated the average degree of water dissociation and its associated free energy at the $SnO_2(110)/H_2O$ interface. Finally, we discuss the PT mechanisms on aqueous rutile oxide interfaces by comparing an oxide series composed of SnO_2, TiO_2, and IrO_2.

COMPUTATIONAL METHODS

AIMD Simulations

The $SnO_2(110)$ surface was built up by a symmetric periodic slab of five O−Sn−O layers with lateral dimensions of a 4 × 2 surface cell (see Figure 1a). The symmetric slabs were separated by a solvent space of 25 Å, giving an orthorhombic supercell with dimensions 12.7 × 13.4 × 41.0 $Å^3$, with the volume of bulk water in the supercell being approximately cubic. The solvent space between the SnO_2 slabs was made up of 143 water molecules, and the number of water molecules was confirmed by adjusting the density of water in the bulk solvent region to ∼1 g/cm^3.

AIMD simulations were performed with the freely available CP2K/Quickstep package.[68,69] The Perdew−Burke−Ernzerhof (PBE) functional was augmented with the D3 dispersion correction of Grimme[70] to properly simulate the $SnO_2(110)/H_2O$ interface. The Goedecker-Teter-Hutter (GTH) pseudopotentials[71,72] were employed to represent the core electrons. The atomic basis sets for the valence electrons ($1s^1$ for H; $2s^2$ and $2p^4$ for O; $5s^2$ and $5p^2$ for Sn) were the standard short-ranged double-ζ basis functions with one set of polarization functions (DZVP).[73] The plane wave cutoff for the electron density expansion was set as 400 Ry. The target accuracy for the SCF convergence was 3×10^{-7} a.u. The NVT ensemble was used for MD propagation with a time step of 0.5 fs, and the equilibrium temperature for all the simulations was kept to 330 K by using the Nosé−Hoover thermostat.[74]

Machine Learning Potential Training

The deep potentials were trained by the open source code DeePMD-kit.[75,76] The Deep Potential-Smooth Edition (DeepPot-SE) model[77] was used for the structural descriptor. The cutoff radius of the local environment was set to 6.0 Å, and the cutoff smooth (rcut_smth) was set as 0.5 Å. To train a practical deep potential, the concurrent learning as implemented in DP-GEN code[78,79] was also applied to construct the data set. In the exploration stage, MD simulations are performed in parallel at the elevated temperatures of 330, 430, and 530 K (Figures S1−S3).

Our final data set contains 600 structures, which were randomly extracted from the 100 ps trajectory of the AIMD simulation, and 5400 structures were collected from concurrent learning. To ensure the quality of DPMD simulations, the final deep potentials in use were trained with 2000000 batch steps, which achieved the L2 energy error of 0.504 meV/atom and the force error of 66.3 meV/Å on the training set (see Figures S4 and S5). In addition, a number of structures were extracted from the trajectory for every 2000 time steps and computed by DFT to validate the accuracy of energies and forces predicted by the deep potentials. The error of energies and forces was 0.8 and 56.8 meV/Å, respectively (Figure S6). The details of deep potential training and the DP-GEN setup are given in the Supporting Information.

DPMD Simulations

The DPMD simulations of the $SnO_2(110)/H_2O$ interface were carried out using the molecular dynamics engine LAMMPS[80] with the same supercell model as AIMD simulations. All the DPMD simulations of the $SnO_2(110)/H_2O$ interface were performed under the canonical ensemble condition (constant volume and constant temperature). The temperature is controlled by the Nosé−Hoover thermostat and is set to 330 K. The MD time step is set to 0.5 fs, and the time scale of DPMD simulation is about 1−5 ns.

CI-NEB Calculations

For SnO_2 covered with a monolayer of adsorbed water, the transition state geometries and energy barriers were studied through the climbing image nudged elastic band (CI-NEB) method[81,82] as implemented in the CP2K code. The transition states were finally verified by the presence of a single imaginary frequency through harmonic vibrational analysis.

RESULTS AND DISCUSSION

Validation and Equilibrium of the $SnO_2(110)/H_2O$ Interface

The radial distribution functions (RDFs) of selected interfacial groups from the 1 ns DPMD trajectory are in excellent agreement with RDFs predicted by 100 ps AIMD simulations for the $SnO_2(110)/H_2O$ interface (Figure 2a). Furthermore, DPMD simulations accurately predict the average water density profile (Figure 2b) and water dipole orientation (Figure 2c), which exhibit perfect symmetry around the center, reflecting the symmetric nature of the interface models. In addition, we find that the vibrational density of state (VDOS) of the O−H groups at the $SnO_2(110)$ surface calculated from AIMD (100 ps) and DPMD (final 100 ps) simulations coincides well, as depicted in Figure 2d. Both the length of simulation trajectories and the length of correlation time used to compute the VDOS from AIMD and DPMD simulations were set as 100 ps. These results indicate that the DPMD simulations have obtained the equilibrium density distribution of interfacial water species at the $SnO_2(110)/H_2O$ interface.

Structure and Proton Transfer at the $SnO_2(110)/H_2O$ Interface

As mentioned in the Introduction, the interfacial groups $Sn_{5c}OH_2$ and Sn_2OH^+ on $SnO_2(110)$ surface have close pK_a values and release protons spontaneously and frequently.[63] In this work, three types of PT pathways are indeed found occurring at the $SnO_2(110)/H_2O$ interface based on AIMD and DPMD simulations (Figure 1b−d). It is worth noting that these three types of PT reactions are reversible due to the close pK_a values for each interfacial group.[63]

The first pathway is proton transfer from terminal water molecule $Sn_{5c}O_aH_2$ to bridge oxygen Sn_2O_{br} directly, which is denoted as "surface-PT" here (Figure 1b):

$$Sn_{5c}O_aH_2\cdots Sn_2O_{br} \rightleftharpoons Sn_{5c}O_aH^-\cdots Sn_2O_{br}H^+ \quad (1)$$

The second pathway involves two terminal groups $Sn_{5c1}O_{a1}H_2$ and $Sn_{5c2}O_{a2}H^-$, which is denoted as "adlayer-PT" (Figure 1c):

$$Sn_{5c1}O_{a1}H_2\cdots Sn_{5c2}O_{a2}H^- \rightleftharpoons Sn_{5c1}O_{a1}H^-\cdots Sn_{5c2}O_{a2}H_2 \quad (2)$$

The third type denoted as "mediated-PT" involves a solvent water molecule H_2O_m between terminal $Sn_{5c}O_aH_2$ and bridge oxygen Sn_2O_{br} (Figure 1d):

$$Sn_{5c}O_aH_2\cdots H_2O_m\cdots Sn_2O_{br} \rightleftharpoons Sn_{5c}O_aH^-\cdots H_2O_m\cdots Sn_2O_{br}H^+ \quad (3)$$

The three types of PT reactions can be viewed as the dissociation (forward reaction) or combination (backward reaction) of the adsorbed water molecule. Previous studies have shown that the pathway of water dissociation is determined by its orientation and the H-bond network.[38,46] Thus, we first analyzed the probability distribution of the average angle θ between the dipole of terminal water and surface normal as demonstrated in Figure 3a.

It is found that the values of θ show three peaks from 0° to 105° (Figure 3a). The first peak is at 38° with both hydrogen atoms of the adsorbed water pointing toward the solution.

https://doi.org/10.1021/prechem.4c00056
Precis. Chem. 2024, 2, 644−654

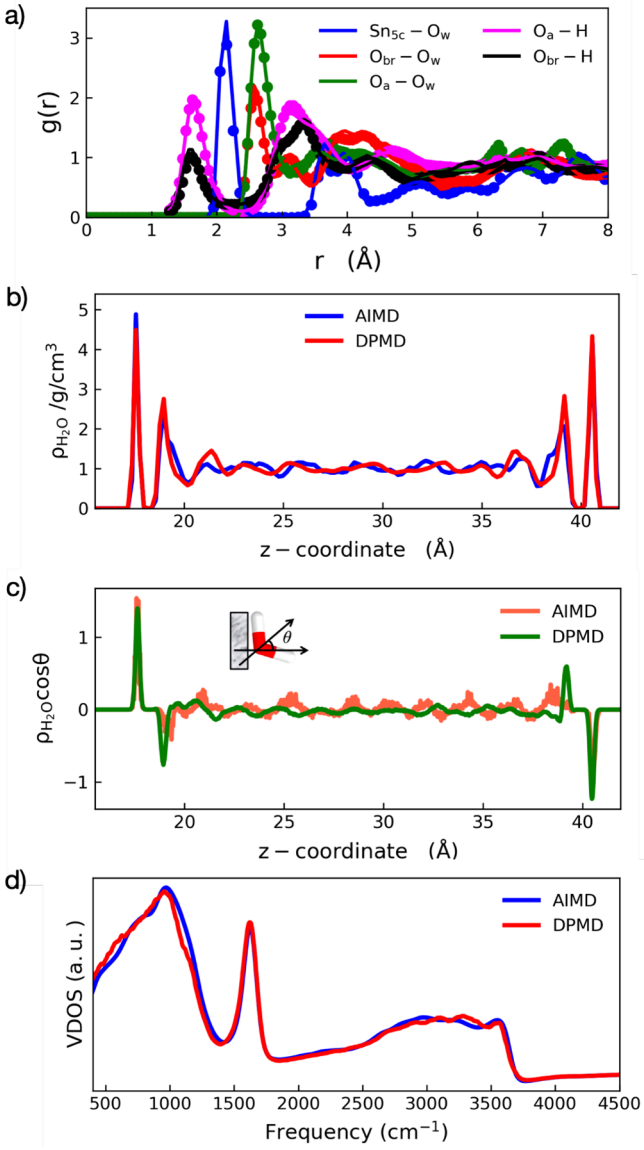

Figure 2. (a) Radial distribution function of selected atomic type pairs at the $SnO_2(110)/H_2O$ interface obtained from DPMD (lines) and AIMD (points). The definitions of Sn_{5c}, O_a, and O_{br} are given in Figure 1, and O_w represents solvent water oxygen atoms. (b,c) Density profiles and dipole orientation of water confined between two SnO_2 surfaces as predicted by DPMD and AIMD simulations. (d) Vibrational density of state (VDOS) of O–H groups at $SnO_2(110)$ surface obtained from AIMD (100 ps) and DPMD (final 100 ps) simulations. We note here that the VDOS were obtained from the Fourier transform of the atomic velocity autocorrelation functions (VACF), and the Fourier transform was smoothed via a Savitzky-Golay filter;[83] a window length of 59 and a polynomial order of 1 were chosen for the filter.

Since the water molecule in this configuration forms two H-bonds with solvent water while donating no H-bond to the interfacial groups, it mainly consists of the mediated-PT as shown in the green box of Figure 3b. The second peak is at 60°, which is also the highest peak, with one hydrogen of the adsorbed water pointing toward the solution and the other parallel to the surface. The former hydrogen forms a hydrogen bond with solvent water, and the latter hydrogen forms a hydrogen bond with the interfacial groups. Note that this kind of terminal water molecule could undergo all three types of PT

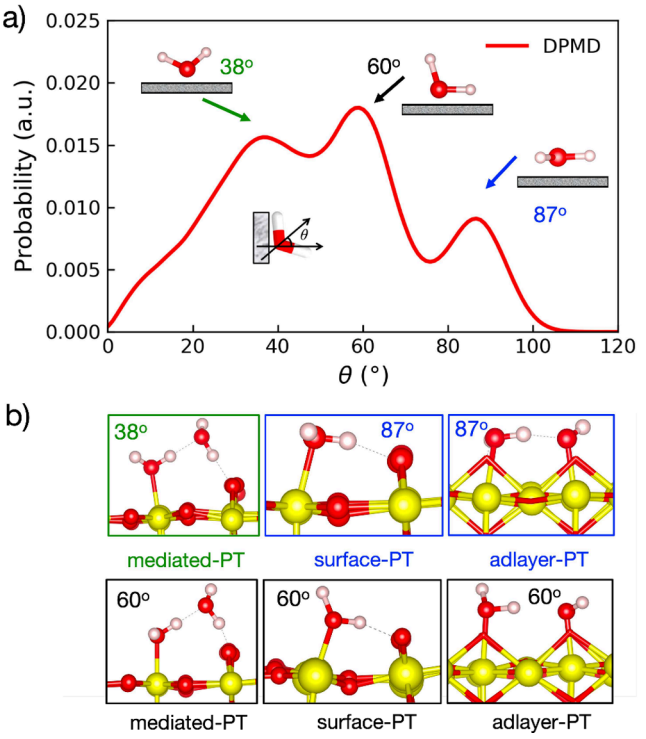

Figure 3. (a) Probability distribution of the angle θ between adsorbed water dipole moment and surface normal for the $SnO_2(110)/H_2O$ interface. (b) Proton transfer pathways correspond to the water orientation in (a) which are distinguished by box color.

reactions at $SnO_2(110)/H_2O$ interface (the black boxes in Figure 3b). The third peak is the smallest peak, which spreads over 87°, suggesting that the adsorbed water molecules are almost parallel to the surface. This water structure forms two H-bonds with interfacial species, and mainly contributes to the surface-PT and adlayer-PT (the blue boxes in Figure 3b).

Free Energy Landscapes of PT Reactions at the $SnO_2(110)/H_2O$ Interface

To further investigate the thermodynamic and kinetic differences among the three types of PT reactions, the free energy landscapes at the $SnO_2(110)/H_2O$ interface are calculated in the following (see Figure 4). By applying the method introduced in ref 84, the free energy profiles of PT reactions are evaluated with the definition of a displacement coordinate δ. The values of δ are defined as $d_{O_a\cdots H_d}$ subtract $d_{O_d\text{-}H_d}$, where $d_{O_a\cdots H_d}$ and $d_{O_d\text{-}H_d}$ are the distances between the donated proton H_d and the two oxygens, i.e., the proton donor O_d and the proton acceptor O_a, in a PT reaction. The one-dimensional PT coordinate δ_{min} is defined by selecting the "most active" H-bond with the minimum of δ, which is most likely to experience PT reactions. When the donated proton O_d is exactly in the middle of O_a and O_d, we can get the $\delta_{min} = 0$ which corresponds to the transition state (TS). The Helmholtz free energy ΔF of a PT reaction can be described as[38]

$$\Delta F(\delta_{min}) = -k_B T \ln W(\delta_{min}) \quad (4)$$

where $W(\delta_{min})$ denotes the counts for the corresponding configuration $HO_d\cdots H_d\cdots O_aH^-$ at a given δ_{min}. The relative rates between two PT reactions i and j can be calculated by the ratio of $W(\delta_{min})$ at the TS ($\delta_{min} = 0$)

https://doi.org/10.1021/prechem.4c00056
Precis. Chem. 2024, 2, 644–654

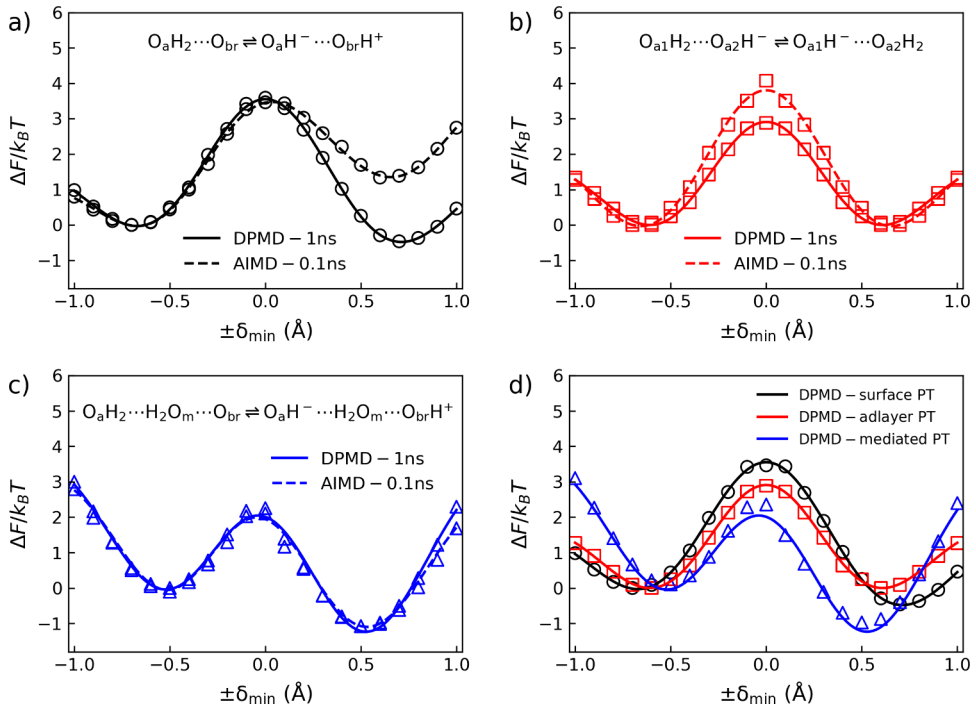

Figure 4. Free energy landscapes for surface-PT (a), adlayer-PT (b), and mediated-PT (c) from AIMD (dashed lines) and DPMD (solid lines) simulations, respectively. (d) Comparison of free energy landscapes for the three PT reactions from DPMD simulations. Note that the free energies ΔF of PT reaction in this figure are calculated from eq 4 and referenced to those of the reactant states for a quick comparison; the origin free energies profiles are shown in Figure S7.

$$\frac{r_i}{r_j} = \frac{W_i(\delta_{min} = 0)}{W_j(\delta_{min} = 0)} \tag{5}$$

To compare the differences between AIMD and DPMD simulations at the $SnO_2(110)/H_2O$ interface, the free energy profiles of the three types of PT reactions based 100 ps AIMD and 1 ns DPMD simulations are calculated using eq 4. As shown in Figure 4, it is found that the mediated-PT has reached equilibrium (Figure 4c) whereas the surface-PT (Figure 4a) and adlayer-PT (Figure 4b) have not reached equilibrium within the 100 ps of AIMD simulation, suggesting that the mediated-PT is the fastest PT reaction at the $SnO_2(110)/H_2O$ interface. The convergences for the free energy profiles of the three PT reactions from DPMD simulations are described in Figures S8–S10. What we observed demonstrates the necessity of employing DPMD simulations to investigate the large free-energy barriers related to slow PT reactions at the oxide/liquid interface.

The energy barriers for the three types of PT reactions from DPMD simulations are listed in Table 1. At the $SnO_2(110)/H_2O$ interface, proton transfer between $Sn_{5c}O_aH_2$ and Sn_2O_{br} sites can be either directly (surface-PT) or indirectly (mediated-PT). It is found that direct surface-PT has the highest energy barrier of 0.10 eV from DPMD simulations (Figure 4a). Interestingly, with the assistance of a solvent water molecule, the mediated-PT has the lowest energy barrier of 0.05 eV (Figure 4c), which is decreased by 50% as compared to surface-PT. For one thing, a smaller average length of H-bond $d_{O_a\cdots H_d}$ (1.46 Å) is observed for the mediated-PT groups along the PT coordinate, as compared to the $d_{O_a\cdots H_d}$ of surface-PT species (1.66 Å). In other words, the donated proton in mediated-PT has a shorter distance to travel (Table 1). For another, the two most abundant angles θ between the adsorbed water dipole and surface normal both at 38° and 60° contributed to mediated-PT (see Figure 3). Therefore, the shorter length of H-bond[85] and the specific orientation of terminal water molecule explain why the mediated-PT barrier is 50% smaller than the surface-PT barrier. Besides, the relative rates between the surface-PT and the mediated-PT can be calculated by eq 5 and given $\frac{r_{mediated-PT}}{r_{surface-PT}} = 28.1$, suggesting that for every surface-PT event, there are 28.1 mediated-PT events.

Moreover, we find that the free energy landscapes for both the surface-PT and the mediated-PT are asymmetric. For the surface-PT, the backward barrier (0.11 eV) is slightly higher than the forward barrier (0.10 eV). Simultaneously, the backward barrier (0.09 eV) is also higher than the forward barrier (0.05 eV) for mediated-PT. Such results suggest that the proton donor group $Sn_{5c}O_aH_2$ is slightly more acidic than Sn_2O_{br} site, which is consistent with the previous calculation of surface acidity constant.[63]

For the adlayer-PT, because the forward and backward PT reactions are equivalent, the free energy barriers are fully symmetric (Figure 4b). When comparing the two direct proton transfer reactions of surface-PT and adlayer-PT, the results

Table 1. Comparison of Water Orientation θ, Length of H-Bonds $d_{Oa\cdots Hd}$ (Å), Energy Barriers (eV), and Relative Rates for Surface-PT, Adlayer-PT, and Mediated-PT from DPMD Simulations

	surface-PT	adlayer-PT	mediated-PT
θ	60°, 87°	60°, 87°	38°, 60°
$d_{O_a\cdots H_d}$	1.66	1.56	1.46
energy barrier	0.10	0.07	0.05
relative PT rate	1	6.9	28.1

https://doi.org/10.1021/prechem.4c00056
Precis. Chem. 2024, 2, 644–654

show the latter has a lower barrier of 0.07 eV because of a shorter average $d_{O_a\cdots H_d}$ (1.56) for adlayer-PT groups along the PT coordinate (see Table 1). The relative rates between surface-PT and adlayer-PT are calculated as $\frac{r_{adlayer-PT}}{r_{surface-PT}} = 6.9$, indicating that, for every surface-PT event, there are 6.9 adlayer-PT events. Hence, the relative PT rates among the three PT reactions at the $SnO_2(110)/H_2O$ interface are $r_{mediated\text{-}PT}:r_{adlayer\text{-}PT}:r_{surface\text{-}PT} = 28.1:6.9:1$.

Full Solvation Effects on Interfacial PT Reactions

It has been known that the solvation environment plays an important role in the interfacial PT reaction.[33,36,86] To further investigate the full solvation effects on interfacial PT reaction, a monolayer of adsorbed water on the $SnO_2(110)$ surface was studied by applying the CI-NEB method. The energy profiles of the three types of PT reactions are shown in Figure 5, and

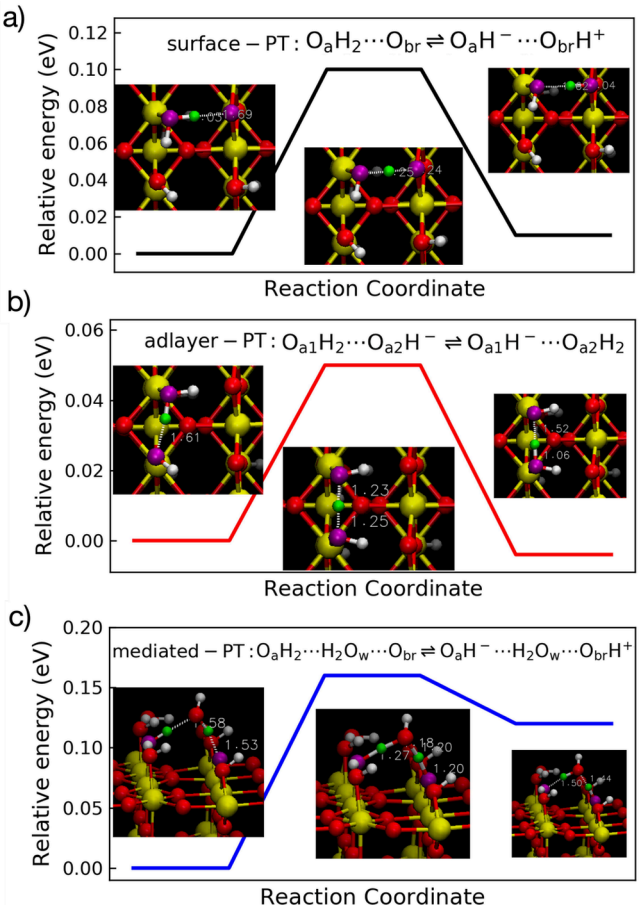

Figure 5. Minimum energy pathway for surface-PT (a), adlayer-PT (b), and mediated-PT (c) reactions calculated by the CI-NEB method, respectively. The Sn, O, and H atoms are colored in yellow, red, and white, respectively. The oxygens and protons involved in the interfacial PT reaction are highlighted in purple and green.

the energy barriers are listed in Table 2. Note that the energy barriers obtained from DPMD simulations and CI-NEB calculations include different entropy effects as well as the definition of reaction coordinate; a rough comparison of energy barriers between the two methods is discussed below.

It is found that the energy barriers of direct surface-PT and adlayer-PT obtained from CI-NEB calculations (Table 2) are almost the same as the DPMD results (Table 1). Based on the

Table 2. Energy Barriers (eV) and Length of H-Bonds $d_{O_a\cdots H_d}$ (Å) Calculated from CI-NEB Calculations with a Monolayer Water Adsorption for Surface-PT, Adlayer-PT, and Mediated-PT[a]

	surface-PT	adlayer-PT	mediated-PT
energy barrier (CI-NEB)	0.10	0.05	0.16
$d_{O_a\cdots H_d}$ (Monolayer)	1.69	1.61	1.58
$\Delta d_{O_a\cdots H_d}$	0.03	0.05	0.12

[a]The difference of $d_{O_a\cdots H_d}$ between full solvation model and monolayer model is denoted as $\Delta\ d_{O_a\cdots H_d}$.

snapshots in the insets of Figure 5a and b, it is observed that the terminal water molecules of monolayer adsorption prefer to be parallel to the surface and form two H-bonds with interfacial species, which correspond to the orientation of the third peak (at 87°) for terminal water in Figure 3a. The differences of $d_{O_a\cdots H_d}$ between DPMD simulations and CI-NEB calculations are only 0.03 and 0.05 Å for surface-PT and adlayer-PT, respectively (see Table 2). In this case, the solvation from solvent water molecules, probably, has little effect on surface-PT and adlayer-PT, which leads to similar energy barriers between the full solvation of DPMD simulations and the monolayer water adsorption of CI-NEB calculations.

However, for the mediated-PT, the terminal water involved in the PT reaction prefers forming one H-bond with solvent water and another with surface species (Figure 5c), which corresponds to the second peak (at 60°) of terminal water orientation in Figure 3a. The difference of $d_{O_a\cdots H_d}$ between DPMD simulation and CI-NEB calculation is 0.12 Å (see Table 2). Without the assistance of the solvation environment, the hydrogen atom of the mediated-water H_2O_m above the SnO_2 surface, which points toward the vacuum, is unstable. This increases the instability of the model system. Therefore, the energy barrier of mediated-PT has increased to 0.16 eV, which is higher than the energy barrier obtained from DPMD simulation (0.05 eV). Through the above general comparison, it is clearly indicated that the solvent water molecules are helpful for the water-mediated proton conduction mechanism at the $SnO_2(110)/H_2O$ interface.

Degree α and Free Energy ΔA_{diss} of Water Dissociation at the $SnO_2(110)/H_2O$ Interface

On the $SnO_2(110)/H_2O$ interface model (Figure 1), there are 8 Sn_{5c} sites and 8 Sn_2O_{br} sites in total. Due to the dissociation of adsorbed water molecules on Sn_{5c} sites, the interfacial species at the $SnO_2(110)$ surface are made up of a mixed state of $Sn_{5c}O_aH_2$, Sn_2O_{br}, $Sn_{5c}O_aH^-$, and $Sn_2O_{br}H^+$. The dissociation of terminal water, which corresponds to surface-PT and mediated-PT, is reversible. The degree of water dissociation α depends on the number of $Sn_{5c}O_aH^-$ group when the $SnO_2(110)/H_2O$ interface achieves dynamic equilibrium. The value of α can be calculated as the ratio of average number of $Sn_{5c}O_aH^-$ group $n(Sn_{5c}O_aH^-)$ to total sites 8, and the values of $n(Sn_{5c}O_aH^-)$ are counted by setting the O−H bond length cutoff as 1.23 Å.

By averaging over the 100 ps AIMD trajectory, it is calculated that the average number of $n(Sn_{5c}O_aH^-)$ is 4.57, and the degree of water dissociation α is estimated to be 0.57 (Table 3). The time cumulative averages of α calculated from AIMD simulations are shown in Figure 6a (black dash line). It

https://doi.org/10.1021/prechem.4c00056
Precis. Chem. 2024, 2, 644−654

Table 3. Comparison of the Average Number of $Sn_{5c}O_aH_2$ and $Sn_{5c}O_aH^-$ Groups, Degree α, and Free Energy of Water Dissociation ΔA_{diss} (Eq 6) from AIMD and DPMD Simulations

	$n(Sn_{5c}O_aH_2)$	$n(Sn_{5c}O_aH^-)$	α	ΔA_{diss} (eV)
AIMD (100 ps)	3.43	4.57	0.57	−0.01
DPMD (5 ns)	3.00	5.00	0.63	−0.03

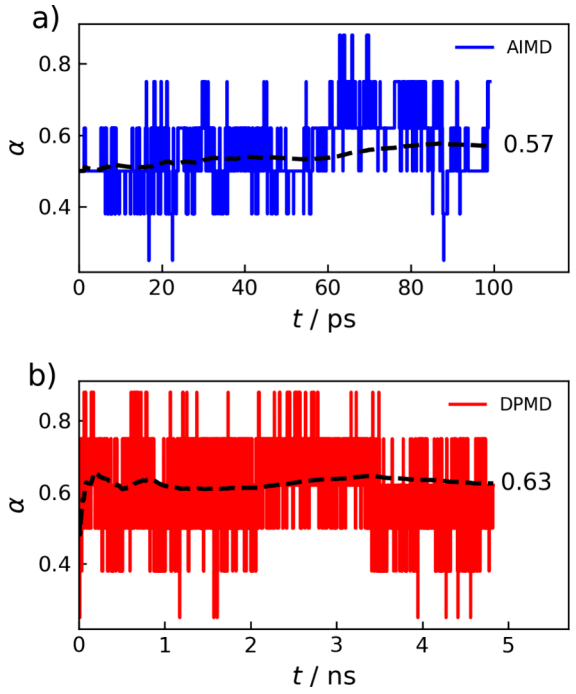

Figure 6. Time evolution of the degree of water dissociation α on the $SnO_2(110)/H_2O$ interface obtained from AIMD (a) and DPMD (b) simulations. The black dashed line is the time average of α.

shows a slightly increasing trend, suggesting that the dynamics of the $SnO_2(110)/H_2O$ interface have not yet obtained equilibrium within the 100 ps time scale. This calls for DPMD simulation, which has reached the equilibrium and validated in Section "Validation and Equilibrium of the $SnO_2(110)/H_2O$ Interface". The value of α is given as 0.62 based on the 1 ns DPMD simulation.

Moreover, to further explore the convergence of α at $SnO_2(110)/H_2O$ interface, the time scale has been extended from 1 to 5 ns by DPMD simulation in this work. The average number of $n(Sn_{5c}O_aH^-)$ is counted as 5.00, and the α is estimated as 0.63 (Table 3), which is consistent with the result of 1 ns (0.62), suggesting that the trajectory of 1 ns DPMD has reached the equilibrium. As shown in Figure 6b, the time cumulative averages of α (black dashed line) remain almost constant within the 5 ns time scale.

The free energy of water dissociation ΔA_{diss} can be linked to the degree of dissociation α

$$\Delta A_{diss} = -k_B T \ln \frac{\alpha^2}{(1-\alpha)^2} \quad (6)$$

The value of ΔA_{diss} is calculated as −0.03 eV based on the 5 ns DPMD simulation from eq 6 (Table 3). The corresponds to almost zero ΔA_{diss} suggests that the proton donor group $Sn_{5c}O_aH_2$ is slightly more acidic than Sn_2O_{br} site, which is consistent with the calculation of free energy landscapes for the fastest mediated-PT shown in Figure 4c.

Comparison of PT Mechanisms on Aqueous Rutile Oxide Interfaces

There are seven types of PT reactions including both direct and indirect pathways among interfacial species that have been reported on oxide surfaces (see Figure 7), i.e., rutile TiO_2,[58,61,86] anatase TiO_2,[51,58] CeO_2,[60] Al_2O_3,[89] ZnO,[38,62] ZrO_2,[36] IrO_2,,[59] AlOOH,[90] InP,[35] and GaP;[35] namely, proton transfer between terminal H_2O and surface oxygen O_s directly (Figure 7a, surface-PT) or via a solvent water molecule (Figure 7b, mediated-PT), proton transfer between two surface oxygens directly (Figure 7c, surface-O_s-PT) or assisted by a solvent water molecule (Figure 7d, solvent-assisted surface-O_s-PT), proton transfer between two terminal groups H_2O and OH^- directly (Figure 7e, adlayer-PT), via a solvent water molecule (Figure 7f, solvent-assisted adlayer-PT-I) or via several solvent water molecules (Figure 7g, solvent-assisted adlayer-PT-II).

For the aqueous isostructural rutile oxide interfaces, one would wonder how adsorbed water would affect the proton hopping mechanisms. To further explore the difference of surface properties and PT pathways for rutile oxide systems, comparison of the ΔpK_a, degree α, and free energy ΔA_{diss} of terminal water dissociation, the water adsorption energy E_{ads}, and PT pathways of a series rutile oxides (SnO_2, TiO_2, and IrO_2) are listed in Table 4. In the dilute limit, the dissociation of terminal water on the oxide surface is determined by the difference ΔpK_a between pK_{a1} (acidity of terminal water) and pK_{a2} (acidity of bridge oxygen).[40,63] It is found the values of ΔpK_a for IrO_2 and SnO_2 are similar, and both are smaller than the TiO_2 surface. Accordingly, the values of α for IrO_2 (0.80[59]) and SnO_2 (0.63) are significantly higher than that for TiO_2 (0.02[52]) (Table 4). Meanwhile, it is found that a positive correlation exists between the water adsorption energy E_{ads} and the degree of terminal water dissociation α, as the $IrO_2(110)$ surface has the highest E_{ads} (−1.92 eV[88]) as well as the highest α (0.80[59]) (Table 4).

For the PT pathways on aqueous rutile oxide interfaces, it is found that only mediated-PT occurs on the $IrO_2(110)$ surface while both surface-PT and mediated-PT go through at TiO_2 and SnO_2 systems. However, the energy barriers of each PT type on TiO_2 and IrO_2 surfaces have not been reported yet, though the overall energy barrier from molecular water to surface hydroxyl on $TiO_2(110)$ surface has been studied.[58] A plausible explanation can be provided based on what we observed on the SnO_2 surface, where the energy barrier of mediated-PT is significantly smaller than the surface-PT, leading to the preference of the mediated-PT pathway on IrO_2 surfaces.

CONCLUSIONS

In summary, by applying a combination of ab initio and deep potential molecular dynamics methods, we have studied the interfacial PT mechanisms by selecting the $SnO_2(110)/H_2O$ interface as an example of rutile oxide with the characteristic of fast PT processes. First, we found three types of PT pathways among the interfacial groups at the $SnO_2(110)/H_2O$ interface: (1) proton transfer from terminal adsorbed water to bridge oxygen directly (surface-PT) or (2) assisted by a solvent water molecule (mediated-PT), and (3) proton transfer between two terminal groups directly (adlayer PT). We calculated the free

https://doi.org/10.1021/prechem.4c00056
Precis. Chem. 2024, 2, 644−654

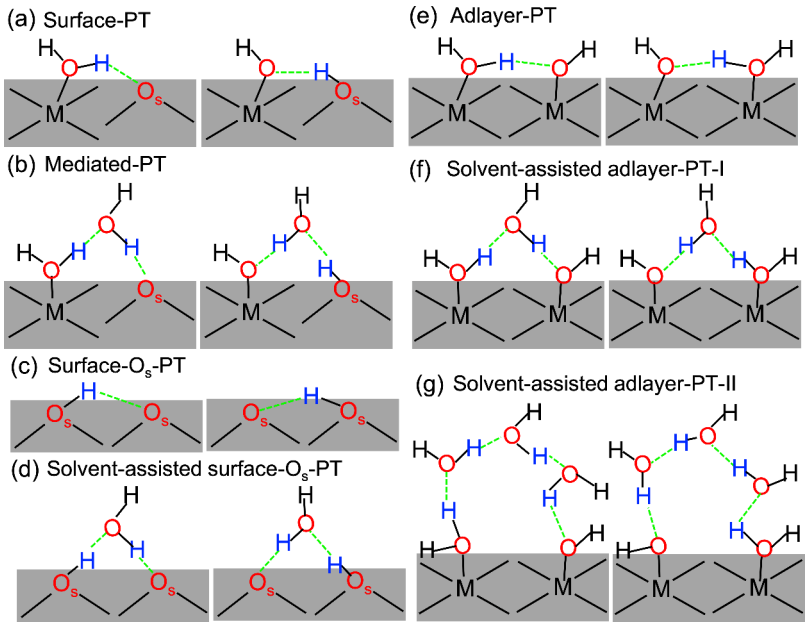

Figure 7. Schematic mechanisms of proton transfer at oxide surfaces which are summarized from the reported literature:[38,51,58−62] proton transfer between terminal H_2O and surface oxygen O_s directly (a) or via a solvent water molecule (b); proton transfer between two surface oxygen atoms directly (c) or assisted by a solvent water molecule (d); proton transfer between two terminal groups H_2O and OH^- directly (e), via a solvent water molecule (f) or via several solvent water molecules (g). The proton donor/acceptor O_d/O_a, the transferred proton, and the H-bond are highlighted in red, blue, and green, respectively.

Table 4. Comparison of ΔpK_a (Acidity Difference between Adsorbed Terminal Water and Protonated Bridge Oxygen $O_{br}H^+$), Degree α, and Free Energy ΔA_{diss} (Obtained from eq 6, eV) of Terminal Water Dissociation, Water Adsorption Energy E_{ads} (eV), and PT Pathways on Rutile $SnO_2(110)$, $TiO_2(110)$, and $IrO_2(110)$ Surfaces

system	ΔpK_a[a]	α[a]	ΔA_{diss}	E_{ads}[b]	PT pathways
$SnO_2(110)/H_2O$	−0.3[63]	0.63	−0.03	−1.5	surface-PT, mediated-PT, adlayer-PT
$TiO_2(110)/H_2O$	3.9[87]	0.020[52]	0.22	−0.87[40]	surface-PT, mediated-PT, adlayer-PT[61]
$IrO_2(110)/H_2O$	−0.4[59]	0.80[59]	−0.08	−1.92[88]	adlayer-PT, water-assisted adlayer-PT, mediated-PT[59]

[a]The results of ΔpK_a and α for SnO_2 and TiO_2 were computed using PBE functional, for IrO_2 was computed using SCAN functional. Note that pK_a's of SnO_2 and TiO_2 were calculated using the free energy perturbation method while the pK_a of IrO_2 was obtained from an enhanced sampling method. [b]The E_{ads} of SnO_2, TiO_2 and IrO_2 were calculated by one monolayer of half dissociated water, molecular water and dissociated water with PBE functional, respectively.

energy landscapes for the three PT reactions and found that the mediated-PT has the lowest energy barrier and the fastest relative PT rate by the assistance of a solvent molecule with a shorter H-bond and a specific orientation of terminal water. Second, we found the full solvation environment plays a crucial role in the water-mediated proton conduction mechanism while having little effect on the direct PT reactions by comparing to the CI-NEB studies of a monolayer of adsorbed water on the $SnO_2(110)$ surface. The average degree of water dissociation α is estimated as 0.63, and the free energy of water dissociation ΔA_{diss} is calculated as −0.03 eV. Finally, we discuss the PT mechanisms on aqueous rutile oxide interfaces by comparing an oxide series composed of SnO_2, TiO_2, and IrO_2. We believe our work provides valuable molecular understanding for proton transfer mechanisms at such heterogeneous oxide interfaces, which is an important step in many chemical processes, including electrocatalysis, heterogeneous catalysis, or other energy production and storage.

■ ASSOCIATED CONTENT

Supporting Information

The Supporting Information is available free of charge at https://pubs.acs.org/doi/10.1021/prechem.4c00056.

Machine learning potential training, comparison of free energy landscapes, and convergence of free energies (PDF)

■ AUTHOR INFORMATION

Corresponding Author

Jun Cheng − *State Key Laboratory of Physical Chemistry of Solid Surfaces, iChEM, College of Chemistry and Chemical Engineering, Xiamen University, Xiamen 361005, China; Laboratory of AI for Electrochemistry (AI4EC), IKKEM, Xiamen 361005, China; Institute of Artificial Intelligence, Xiamen University, Xiamen 361005, China;* orcid.org/0000-0001-6971-0797; Email: chengjun@xmu.edu.cn

Authors

Mei Jia − *Henan Key Laboratory of Biomolecular Recognition and Sensing, Henan Joint International Research Laboratory of Chemo/Biosensing and Early Diagnosis of Major Diseases, College of Chemistry and Chemical Engineering, Shangqiu Normal University, Shangqiu 476000, China; State Key Laboratory of Physical Chemistry of Solid Surfaces, iChEM, College of Chemistry and Chemical Engineering, Xiamen University, Xiamen 361005, China*

https://doi.org/10.1021/prechem.4c00056
Precis. Chem. 2024, 2, 644−654

Yong-Bin Zhuang − *State Key Laboratory of Physical Chemistry of Solid Surfaces, iChEM, College of Chemistry and Chemical Engineering, Xiamen University, Xiamen 361005, China;* Present Address: Chaire de Simulation à l'Échelle Atomique (CSEA), Ecole Polytechnique Fédérale de Lausanne (EPFL), CH-1015 Lausanne, Switzerland; orcid.org/0000-0001-5182-8084

Feng Wang − *State Key Laboratory of Physical Chemistry of Solid Surfaces, iChEM, College of Chemistry and Chemical Engineering, Xiamen University, Xiamen 361005, China*

Chao Zhang − *Department of Chemistry-Ångström Laboratory, Uppsala University, 75121 Uppsala, Sweden;* orcid.org/0000-0002-7167-0840

Complete contact information is available at: https://pubs.acs.org/10.1021/prechem.4c00056

Author Contributions

#M.J. and Y.-B.Z. contributed equally to this work. J.C. and M.J. conceived and designed the project, M J. performed the AIMD calculations and analyzed the data, and Y.-B.Z. performed the DPMD calculations. The first draft of the manuscript was prepared by M.J. and Y.-B.Z., and the final draft was edited by all the authors.

Notes

The authors declare no competing financial interest.

■ ACKNOWLEDGMENTS

J.C. gratefully acknowledges funding from the National Science Fund for Distinguished Young Scholars (Grant No. 22225302), the National Natural Science Foundation of China (Grant Nos. 92161113, 21991151, 21991150, and 22021001) and the Fundamental Research Funds for the Central Universities (Grant Nos. 20720220008, 20720220009, 20720220010), Laboratory of AI for Electrochemistry (AI4EC), and IKKEM (Grant Nos. RD2023100101 and RD2022070501). M.J. greatly appreciates the financial support from the Natural Science Foundation of Henan Province (Grant No. 242300420420570), the Key Scientific Research Projects of Colleges and Universities in Henan Province (No. 24A150031), and the International Scientific and Technological Cooperation Projects in Henan Province (No. 232102520020). Y.-B.Z. acknowledges Xiamen University and iChEM for a Ph.D. studentship. We thank Y.-M Wang for drawing the cartoon characters in graphical TOC.

■ REFERENCES

(1) Augustyn, V.; Simon, P.; Dunn, B. Pseudocapacitive oxide materials for high-rate electrochemical energy storage. *Energy Environ. Sci.* **2014**, *7*, 1597−1614.

(2) Zhang, H.; Chen, G.; Bahnemann, D. W. Photoelectrocatalytic materials for environmental applications. *J. Mater. Chem.* **2009**, *19*, 5089−5121.

(3) Stumm, W. Reactivity at the mineral-water interface: dissolution and inhibition. *Colloids Surf., A* **1997**, *120*, 143−166.

(4) Weir, A.; Westerhoff, P.; Fabricius, L.; Hristovski, K.; von Goetz, N. Titanium Dioxide Nanoparticles in Food and Personal Care Products. *Environ. Sci. Technol.* **2012**, *46*, 2242−2250.

(5) Hiemstra, T.; Van Riemsdijk, W. Surface structural ion adsorption modeling of competitive binding of oxyanions by metal (hydr)oxides. *J. Colloid Interface Sci.* **1999**, *210*, 182−193.

(6) Tamura, H.; Mita, K.; Tanaka, A.; Ito, M. Mechanism of hydroxylation of metal oxide surfaces. *J. Colloid Interface Sci.* **2001**, *243*, 202−207.

(7) Pham, T. A.; Lee, D.; Schwegler, E.; Galli, G. Interfacial Effects on the Band Edges of Functionalized Si Surfaces in Liquid Water. *J. Am. Chem. Soc.* **2014**, *136*, 17071−17077.

(8) Ardizzone, S.; Trasatti, S. Interfacial properties of oxides with technological impact in electrochemistry. *Adv. Colloid Interface Sci.* **1996**, *64*, 173−251.

(9) Brown, G. E.; Henrich, V. E.; Casey, W. H.; Clark, D. L.; Eggleston, C.; Felmy, A.; Goodman, D. W.; Grätzel, M.; Maciel, G.; McCarthy, M. I.; Nealson, K. H.; Sverjensky, D. A.; Toney, M. F.; Zachara, J. M. Metal Oxide Surfaces and Their Interactions with Aqueous Solutions and Microbial Organisms. *Chem. Rev.* **1999**, *99*, 77−174.

(10) Schmickler, W.; Santos, E. *Interfacial Electrochemistry*; Springer: Berlin, 2010.

(11) Stumm, W. *Chemistry of the Solid−Water Interface*; Wiley: New York, 1992.

(12) Weinberg, D. R.; Gagliardi, C. J.; Hull, J. F.; Murphy, C. F.; Kent, C. A.; Westlake, B. C.; Paul, A.; Ess, D. H.; McCafferty, D. G.; Meyer, T. J. Proton-Coupled Electron Transfer. *Chem. Rev.* **2012**, *112*, 4016−4093.

(13) Huynh, M. H. V.; Meyer, T. J. Proton-coupled electron transfer. *Chem. Rev.* **2007**, *107*, 5004−5064.

(14) Chinese Society of Electrochemistry. The Top Ten Scientific Questions in Electrochemistry. *J. Electrochem.* **2024**, *30*, 2024121.

(15) Khan, S.; Al-Shahry, M.; Ingler, W. Efficient photochemical water splitting by a chemically modified n-TiO2. *Science* **2002**, *297*, 2243−2245.

(16) Cheng, J.; Liu, X.; Kattirtzi, J. A.; VandeVondele, J.; Sprik, M. Aligning Electronic and Protonic Energy Levels of Proton-Coupled Electron Transfer in Water Oxidation on Aqueous TiO2. *Angew. Chem., Int. Ed.* **2014**, *53*, 12046−12050.

(17) Cortright, R.; Davda, R.; Dumesic, J. Hydrogen from catalytic reforming of biomass-derived hydrocarbons in liquid water. *Nature* **2002**, *418*, 964−967.

(18) Ait-Ichou, I.; Formenti, M.; Pommier, B.; Teichner, S. Photocatalytic dehydrogenation of isopropanol on $PtTiO_2$ catalysts. *J. Catal.* **1985**, *91*, 293−307.

(19) Cheng, H.; Chen, L.; Cooper, A. C.; Sha, X.; Pez, G. P. Hydrogen spillover in the context of hydrogen storage using solid-state materials. *Energy Environ. Sci.* **2008**, *1*, 338−354.

(20) Du, Q.; Freysz, E.; Shen, Y. R. Surface vibrational spectroscopic studies of hydrogen bonding and hydrophobicity. *Science* **1994**, *264*, 826−828.

(21) Chu, Y.; Lister, T.; Cullen, W.; You, H.; Nagy, Z. Commensurate water monolayer at the RuO2(110)/water interface. *Phys. Rev. Lett.* **2001**, *86*, 3364−3367.

(22) Yamamoto, S.; Bluhm, H.; Andersson, K.; Ketteler, G.; Ogasawara, H.; Salmeron, M.; Nilsson, A. In situ x-ray photoelectron spectroscopy studies of water on metals and oxides at ambient conditions. *J. Phys.: Condens. Matter* **2008**, *20*, 184025.

(23) van Oversteeg, C. H. M.; Doan, H. Q.; de Groot, F. M. F.; Cuk, T. In situ X-ray absorption spectroscopy of transition metal based water oxidation catalysts. *Chem. Soc. Rev.* **2017**, *46*, 102−125.

(24) Santos, J. C. C.; Negreiros, F. R.; Pedroza, L. S.; Dalpian, G. M.; Miranda, P. B. Interaction of Water with the Gypsum (010) Surface: Structure and Dynamics from Nonlinear Vibrational Spectroscopy and Ab Initio Molecular Dynamics. *J. Am. Chem. Soc.* **2018**, *140*, 17141−17152.

(25) Khatib, R.; Backus, E. H. G.; Bonn, M.; Perez-Haro, M.-J.; Gaigeot, M.-P.; Sulpizi, M. Water orientation and hydrogen-bond structure at the fluorite/water interface. *Sci. Rep.* **2016**, *6*, 24287.

(26) Lesnicki, D.; Zhang, Z.; Bonn, M.; Sulpizi, M.; Backus, E. H. Surface Charges at the CaF2/Water Interface Allow Very Fast Intermolecular Vibrational-Energy Transfer. *Angew. Chem., Int. Ed.* **2020**, *59*, 13116−13121.

(27) Ohno, P. E.; Saslow, S. A.; Wang, H.-F.; Geiger, F. M.; Eisenthal, K. B. Phase-referenced nonlinear spectroscopy of the α-quartz/water interface. *Nat. Commun.* **2016**, *7*, 13587.

(28) Ren, B.; Li, J.-F.; Huang, Y.-F.; Zeng, Z.-C.; Tian, Z.-Q. Electrochemical Surface-Enhanced Raman Spectroscopy—Current Status and Perspective. *J. Electrochem.* **2010**, *16*, 305.
(29) Li, C.-Y.; Le, J.-B.; Wang, Y.-H.; Chen, S.; Yang, Z.-L.; Li, J.-F.; Cheng, J.; Tian, Z.-Q. In situ probing electrified interfacial water structures at atomically flat surfaces. *Nature materials* **2019**, *18*, 697−701.
(30) Yang, Y.-Y.; Zhang, H.-X.; Cai, W.-B. Recent experimental progresses on electrochemical ATR-SEIRAS. *J. Electrochem.* **2013**, *19*, 1.
(31) Mu, R.; Cantu, D. C.; Lin, X.; Glezakou, V.-A.; Wang, Z.; Lyubinetsky, I.; Rousseau, R.; Dohnalek, Z. Dimerization Induced Deprotonation of Water on RuO2(110). *J. Phys. Chem. Lett.* **2014**, *5*, 3445−3450.
(32) Hussain, H.; Tocci, G.; Woolcot, T.; Torrelles, X.; Pang, C. L.; Humphrey, D. S.; Yim, C. M.; Grinter, D. C.; Cabailh, G.; Bikondoa, O.; Lindsay, R.; Zegenhagen, J.; Michaelides, A.; Thornton, G. Structure of a model TiO2 photocatalytic interface. *Nat. Mater.* **2017**, *16*, 461.
(33) Merte, L. R.; Peng, G.; Bechstein, R.; Rieboldt, F.; Farberow, C. A.; Grabow, L. C.; Kudernatsch, W.; Wendt, S.; Laegsgaard, E.; Mavrikakis, M.; Besenbacher, F. Water-Mediated Proton Hopping on an Iron Oxide Surface. *Science* **2012**, *336*, 889−893.
(34) Zhang, C.; Hutter, J.; Sprik, M. Coupling of Surface Chemistry and Electric Double Layer at TiO_2 Electrochemical Interfaces. *J. Phys. Chem. Lett.* **2019**, *10*, 3871−3876.
(35) Wood, B. C.; Schwegler, E.; Choi, W. I.; Ogitsu, T. Hydrogen-Bond Dynamics of Water at the Interface with InP/GaP(001) and the Implications for Photoelectrochemistry. *J. Am. Chem. Soc.* **2013**, *135*, 15774−15783.
(36) Sato, R.; Ohkuma, S.; Shibuta, Y.; Shimojo, F.; Yamaguchi, S. Proton Migration on Hydrated Surface of Cubic ZrO2: Ab initio Molecular Dynamics Simulation. *J. Phys. Chem. C* **2015**, *119*, 28925−28933.
(37) Tocci, G.; Michaelides, A. Solvent-Induced Proton Hopping at a Water-Oxide Interface. *J. Phys. Chem. Lett.* **2014**, *5*, 474−480.
(38) Quaranta, V.; Hellström, M.; Behler, J. Proton-transfer mechanisms at the water-ZnO interface: the role of presolvation. *J. Phys. Chem. Lett.* **2017**, *8*, 1476−1483.
(39) Lentz, J.; Garofalini, S. H. Role of the hydrogen bond lifetimes and rotations at the water/amorphous silica interface on proton transport. *Phys. Chem. Chem. Phys.* **2019**, *21*, 12265−12278.
(40) Cheng, J.; Sprik, M. Acidity of the Aqueous Rutile TiO_2(110) Surface from Density Functional Theory Based Molecular Dynamics. *J. Chem. Theory Comput.* **2010**, *6*, 880.
(41) Zhuang, Y.-B.; Cheng, J. Band Alignments of Metal/Oxides-Water Interfaces Using Ab Initio Molecular Dynamics. *J. Electrochem.* **2023**, *29*, 3.
(42) Rosenqvist, J.; Machesky, M. L.; Vlcek, L.; Cummings, P. T.; Wesolowski, D. J. Charging properties of cassiterite (α-SnO_2) surfaces in NaCl and RbCl ionic media. *Langmuir* **2009**, *25*, 10852−10862.
(43) Machesky, M. L.; Předota, M.; Wesolowski, D. J.; Vlcek, L.; Cummings, P. T.; Rosenqvist, J.; Ridley, M. K.; Kubicki, J. D.; Bandura, A. V.; Kumar, N.; Sofo, J. O. Surface protonation at the rutile (110) interface: Explicit incorporation of solvation structure within the refined MUSIC model framework. *Langmuir* **2008**, *24*, 12331−12339.
(44) Vlcek, L.; Zhang, Z.; Machesky, M. L.; Fenter, P.; Rosenqvist, J.; Wesolowski, D. J.; Anovitz, L. M.; Predota, M.; Cummings, P. T. Electric double layer at metal oxide surfaces: Static properties of the cassiterite-water interface. *Langmuir* **2007**, *23*, 4925−4937.
(45) Cheng, J.; Liu, X.; VandeVondele, J.; Sulpizi, M.; Sprik, M. Redox potentials and acidity constants from density functional theory based molecular dynamics. *Acc. Chem. Res.* **2014**, *47*, 3522−3529.
(46) Fan, X.-T.; Wen, X.-J.; Zhuang, Y.-B.; Cheng, J. Molecular insight into the GaP (110)−water interface using machine learning accelerated molecular dynamics. *J. Energy Chem.* **2023**, *82*, 239−247.
(47) Zhang, L.; Han, J.; Wang, H.; Car, R.; E, W. Deep Potential Molecular Dynamics: A Scalable Model with the Accuracy of Quantum Mechanics. *Phys. Rev. Lett.* **2018**, *120*, 143001.
(48) Behler, J.; Parrinello, M. Generalized Neural-Network Representation of High-Dimensional Potential-Energy Surfaces. *Phys. Rev. Lett.* **2007**, *98*, 146401.
(49) Bartók, A. P.; Payne, M. C.; Kondor, R.; Csányi, G. Gaussian Approximation Potentials: The Accuracy of Quantum Mechanics, without the Electrons. *Phys. Rev. Lett.* **2010**, *104*, 136403.
(50) Jia, W.; Wang, H.; Chen, M.; Lu, D.; Lin, L.; Car, R.; Weinan, E.; Zhang, L. Pushing the limit of molecular dynamics with ab initio accuracy to 100 million atoms with machine learning. *SC20: International conference for high performance computing, networking, storage and analysis*; 2020; pp 1−14.
(51) Calegari Andrade, M. F.; Ko, H.-Y.; Zhang, L.; Car, R.; Selloni, A. Free energy of proton transfer at the water-TiO2 interface from ab initio deep potential molecular dynamics. *Chem. Sci.* **2020**, *11*, 2335−2341.
(52) Zhuang, Y.-B.; Bi, R.-H.; Cheng, J. Resolving the odd−even oscillation of water dissociation at rutile TiO2(110)-water interface by machine learning accelerated molecular dynamics. *J. Chem. Phys.* **2022**, *157*, 164701.
(53) Zhuang, Y.-B.; Cheng, J. Deciphering the anomalous acidic tendency of terminal water at rutile(110)-water interfaces. *J. Phys. Chem. C* **2023**, *127*, 10532−10540.
(54) Wang, F.; Cheng, J. Automated workflow for redox potentials and acidity constants calculations from machine learning molecular dynamics. *J. Electrochem.* **2024**, *30*, 2.
(55) Torrie, G. M.; Valleau, J. P. Nonphysical sampling distributions in Monte Carlo free-energy estimation: Umbrella sampling. *J. Comput. Phys.* **1977**, *23*, 187−199.
(56) Barducci, A.; Bussi, G.; Parrinello, M. Well-tempered metadynamics: a smoothly converging and tunable free-energy method. *Phys. Rev. Lett.* **2008**, *100*, 020603.
(57) Grifoni, E.; Piccini, G.; Parrinello, M. Microscopic description of acid−base equilibrium. *Proc. Natl. Acad. Sci. U. S. A.* **2019**, *116*, 4054−4057.
(58) Zeng, Z.; Wodaczek, F.; Liu, K.; Stein, F.; Hutter, J.; Chen, J.; Cheng, B. Mechanistic insight on water dissociation on pristine low-index TiO2 surfaces from machine learning molecular dynamics simulations. *Nat. Commun.* **2023**, *14*, 6131.
(59) Raman, A. S.; Selloni, A. Acid−base chemistry of a model IrO2 catalytic interface. *J. Phys. Chem. Lett.* **2023**, *14*, 7787−7794.
(60) Kobayashi, T.; Ikeda, T.; Nakayama, A. Long-range proton and hydroxide ion transfer dynamics at the water/CeO2 interface in the nanosecond regime: reactive molecular dynamics simulations and kinetic analysis. *Chem. Sci.* **2024**, *15*, 6816−6832.
(61) Wen, B.; Calegari Andrade, M. F.; Liu, L.-M.; Selloni, A. Water dissociation at the water−rutile TiO2 (110) interface from ab initio-based deep neural network simulations. *Proc. Natl. Acad. Sci. U. S. A.* **2023**, *120*, No. e2212250120.
(62) Quaranta, V.; Behler, J.; Hellström, M. Structure and dynamics of the liquid−water/zinc-oxide interface from machine learning potential simulations. *J. Phys. Chem. C* **2019**, *123*, 1293−1304.
(63) Jia, M.; Zhang, C.; Cox, S. J.; Sprik, M.; Cheng, J. Computing surface acidity constants of proton hopping groups from Density Functional Theory-based Molecular Dynamics: application to the SnO2(110)/H2O interface. *J. Chem. Theory Comput.* **2020**, *16*, 6520−6527.
(64) Hu, C.; Chen, L.; Hu, Y.; Chen, A.; Chen, L.; Jiang, H.; Li, C. Light-motivated SnO2/TiO2 heterojunctions enabling the breakthrough in energy density for lithium-ion batteries. *Adv. Mater.* **2021**, *33*, 2103558.
(65) Guo, Z.; Yu, Y.; Li, C.; Campos dos Santos, E.; Wang, T.; Li, H.; Xu, J.; Liu, C.; Li, H. Deciphering structure-activity relationship towards CO2 electroreduction over SnO2 by a standard research paradigm. *Angew. Chem., Int. Ed.* **2024**, *63*, No. e202319913.
(66) Yan, X.; Liu, W.; Kang, H.; Zhang, S.; Shi, S. Self-standing 3D hollow nanoporous SnO2-modified CuxO nanotubes with nano-

lamellar metallic Cu inwalls: a facile in situ synthesis protocol toward enhanced Li storage properties. *Adv. Funct. Mater.* **2023**, *33*, 2212654.
(67) Li, C.; Choi, P. G.; Masuda, Y. Large-lateral-area SnO2 nanosheets with a loose structure for high-performance acetone sensor at the ppt level. *J. Hazard. Mater.* **2023**, *455*, 131592.
(68) Hutter, J.; Iannuzzi, M.; Schiffmann, F.; VandeVondele, J. CP2K: atomistic simulations of condensed matter systems. *Wiley Interdiscip. Rev.: Comput. Mol. Sci.* **2014**, *4*, 15−25.
(69) VandeVondele, J.; Krack, M.; Mohamed, F.; Parrinello, M.; Chassaing, T.; Hutter, J. Quickstep: Fast and accurate density functional calculations using a mixed Gaussian and plane waves approach. *Comput. Phys. Commun.* **2005**, *167*, 103−128.
(70) Grimme, S.; Antony, J.; Ehrlich, S.; Krieg, H. A consistent and accurate ab initio parametrization of density functional dispersion correction (DFT-D) for the 94 elements H-Pu. *J. Chem. Phys.* **2010**, *132*, 154104.
(71) Hartwigsen, C.; Goedecker, S.; Hutter, J. Relativistic separable dual-space Gaussian pseudopotentials from H to Rn. *Phys. Rev. B* **1998**, *58*, 3641−3662.
(72) Goedecker, S.; Teter, M.; Hutter, J. Separable dual-space Gaussian pseudopotentials. *Phys. Rev. B* **1996**, *54*, 1703−1710.
(73) VandeVondele, J.; Hutter, J. Gaussian basis sets for accurate calculations on molecular systems in gas and condensed phases. *J. Chem. Phys.* **2007**, *127*, 114105.
(74) VandeVondele, J.; Mohamed, F.; Krack, M.; Hutter, J.; Sprik, M.; Parrinello, M. The influence of temperature and density functional models in ab initio molecular dynamics simulation of liquid water. *J. Chem. Phys.* **2005**, *122*, 014515.
(75) Wang, H.; Zhang, L.; Han, J.; E, W. DeePMD-kit: A deep learning package for many-body potential energy representation and molecular dynamics. *Comput. Phys. Commun.* **2018**, *228*, 178−184.
(76) Zeng, J.-Z.; et al. DeePMD-kit v2: A software package for deep potential models. *J. Chem. Phys.* **2023**, *159*, 054801.
(77) Zhang, L.; Han, J.; Wang, H.; Saidi, W.; Car, R.; E, W. End-to-end symmetry preserving inter-atomic potential energy model for finite and extended systems. *Advances in Neural Information Processing Systems* **2018**, 4441.
(78) Zhang, L.; Lin, D.-Y. Y.; Wang, H.; Car, R.; E, W.; Weinan, E. Active learning of uniformly accurate interatomic potentials for materials simulation. *Phys. Rev. Mater.* **2019**, *3*, 023804.
(79) Zhang, Y.; Wang, H.; Chen, W.; Zeng, J.; Zhang, L.; Wang, H.; E, W. DP-GEN: A concurrent learning platform for the generation of reliable deep learning based potential energy models. *Comput. Phys. Commun.* **2020**, *253*, 107206.
(80) Thompson, A. P.; Aktulga, H. M.; Berger, R.; Bolintineanu, D. S.; Brown, W. M.; Crozier, P. S.; in 't Veld, P. J.; Kohlmeyer, A.; Moore, S. G.; Nguyen, T. D.; Shan, R.; Stevens, M. J.; Tranchida, J.; Trott, C.; Plimpton, S. J. LAMMPS - a flexible simulation tool for particle-based materials modeling at the atomic, meso, and continuum scales. *Comput. Phys. Commun.* **2022**, *271*, 108171.
(81) Henkelman, G.; Uberuaga, B. P.; Jonsson, H. A climbing image nudged elastic band method for finding saddle points and minimum energy paths. *J. Chem. Phys.* **2000**, *113*, 9901−9904.
(82) Henkelman, G.; Jonsson, H. Improved tangent estimate in the nudged elastic band method for finding minimum energy paths and saddle points. *J. Chem. Phys.* **2000**, *113*, 9978−9985.
(83) Savitzky, A.; Golay, M. J. Smoothing and differentiation of data by simplified least squares procedures. *Anal. Chem.* **1964**, *36*, 1627−1639.
(84) Tuckerman, M.; Marx, D.; Parrinello, M. The nature and transport mechanism of hydrated hydroxide ions in aqueous solution. *Nature* **2002**, *417*, 925−929.
(85) Benoit, M.; Marx, D. The shapes of protons in hydrogen bonds depend on the bond length. *ChemPhysChem* **2005**, *6*, 1738−1741.
(86) Agosta, L.; Brandt, E. G.; Lyubartsev, A. P. Diffusion and reaction pathways of water near fully hydrated TiO2 surfaces from ab initio molecular dynamics. *J. Chem. Phys.* **2017**, *147*, 024704.
(87) Cheng, J.; Liu, X.; VandeVondele, J.; Sprik, M. Reductive hydrogenation of the aqueous rutile TiO2 (110) surface. *Electrochim. Acta* **2015**, *179*, 658−667.
(88) Zhao, F.; Wen, B.; Niu, W.; Chen, Z.; Yan, C.; Selloni, A.; Tully, C. G.; Yang, X.; Koel, B. E. Increasing iridium oxide activity for the oxygen evolution reaction with hafnium modification. *J. Am. Chem. Soc.* **2021**, *143*, 15616−15623.
(89) Ridley, M. K.; Tunega, D. Insights on the structural and dynamic properties of corundum−water interfaces from first-principle molecular dynamics. *J. Phys. Chem. C* **2021**, *125*, 295−309.
(90) Motta, A.; Gaigeot, M.-P.; Costa, D. Ab Initio Molecular Dynamics Study of the AlOOH Boehmite/Water Interface: Role of Steps in Interfacial Grotthus Proton Transfers. *J. Phys. Chem. C* **2012**, *116*, 12514−12524.

https://doi.org/10.1021/prechem.4c00056
Precis. Chem. 2024, 2, 644−654